Lithosphere

Research Article

Low-Crystallinity Index Chalcedony from Longhua, China: Characteristics and Formation

Qiuli Yan[1] and Guanghai Shi🄳[1,2]

[1]*School of Gemology, China University of Geosciences, Beijing, 100083, China*
[2]*State Key Laboratory of Geological Processes and Mineral Resources, China University of Geosciences, Beijing, 100083, China*

Correspondence should be addressed to Guanghai Shi; shigh@cugb.edu.cn

A low-crystallinity index chalcedony was found in the rhyolitic ignimbrite of the Late Jurassic Zhangjiakou Formation, located in Longhua County, Hebei Province, China. This chalcedony occurs as fillings along the fragile fractures of the host rock and is distinct from any other chalcedony deposits, such as the known basalt and carbonate-related types. The host rock is rhyolitic ignimbrite, comprising sanidine (50–70 vol.%), plagioclase (10–15 vol.%), quartz (8–10 vol.%), magnesian biotite (3–5 vol.%), and accessory minerals. The chalcedony appears as long lenticular veins and irregular-shaped bodies, occasionally containing small fragments of the surrounding rock at the boundary. It is colored in yellow, red, and/or white/colorless, with physical properties of specific gravity 2.55–2.56, reflection index of 1.54, Mohs hardness of 6.07–6.34, and weight loss of 1.97%–2.32% by heating. From the boundary to the inner center, its growth structure changes from comb-like macrocrystalline quartz to thin fiber crystallites and then to a relatively uniform cryptocrystalline phase, indicating precipitation from a crystalline to the cryptocrystalline sequence. Electron probe and Raman spectroscopy analyses reveal that the component minerals of the chalcedony are α-quartz and moganite and that the red inclusions are hematite. Quartz in chalcedony exhibits platelet shapes with tiny pores, which are cemented by nanograins, and such a structure is closer to that of opal. It's crystallinity indexes (CIs) range ~1–3, as indicated by the X-ray diffraction patterns. This low CI and structural features, together with its occurrence, suggest a low temperature of 40°C–80°C during its formation. All these properties show a distinction from those of the most reported chalcedonies. This chalcedony is interpreted as an intermediate transitional type from normal chalcedony to opal, shedding new light on understanding microcrystalline silica mineral aggregate and exploration for a similar gem deposit.

1. Introduction

Silica minerals are widespread on Earth and could be classified into three types: macrocrystalline, microcrystalline, and noncrystalline based on microstructure and characteristic properties. From real macrocrystal silica to microcrystalline one, obvious trends of decreasing particle size and increasing influence of particle surfaces exist. To noncrystalline silica, whatever from macrocrystalline and/or microcrystalline phase, an increasing structural disorder is distinctive [1, 2]. According to the nomenclature of silica minerals [1], microcrystalline silica minerals could be further classified into low-quartz (microquartz, chalcedony, and quartzine), moganite, cristobalite, and tridymite (opal-C and opal-CT). Noncrystalline silica minerals are classified into opal-A, noncrystalline silica with characteristic amounts of water, and lechâtelierite, silica-glass almost free of water.

Chalcedony is one of the most famous and widespread microcrystalline silica minerals. In addition, banded chalcedony is known as agate, which represents a mixture of silica polymorphs. Chalcedony and agate are popular gemstones in the jewelry market due to their various colors and charming patterns. Chalcedonies are mostly

composed of low α-quartz and moganite, but some of them may also contain minor opaline-quartz phases and mineral inclusions [3–5]. Chalcedonies and agates have been described from various regions, and their occurrences are connected with practically all rock types [6–9]. In acidic volcanic rocks, agate is mostly produced as spheroids, formed in cavities, with a few being vein-shaped [10]. Studies have suggested that the structure of chalcedony is stacked silica plates [11]. For a certain veined agate, its outermost layer is usually composed of a cryptocrystalline silica phase, whereas the innermost layer is euhedral quartz [12]. However, new occurrences and/or various appearances of chalcedonies occasionally appear, and attentions have been paid consequently [13–15].

Recently, a low-crystallinity index chalcedony was found within rhyolitic ignimbrite in Longhua County, China, and is noteworthy both in mineralogy and gemology. In this study, we utilized approaches integrating petrographic observation, mineral chemistry, oxygen isotope, and Raman microanalysis to examine the characteristics of chalcedony and the related rocks. We demonstrated the possible petrogenesis and gemological applications. Based on field investigations and analyses, we propose that the low-crystallinity chalcedony was formed through a stratification precipitation mechanism. The chalcedony, as a rare gem in ignimbrite, implies that microcrystalline silica minerals might have more occurrences and appearances undiscovered and thus have potential implications in the economy as well.

2. Geological Setting

The chalcedony deposit (Figure 1(a)) is located at the northern margin of the North China Craton within the middle part of the Yanshanian orogenic belt [16, 17]. Previous studies have suggested that the study area underwent a transition of the tectonic regime between the paleo-Asian Ocean tectonic system and the paleo-Pacific tectonic system in the Mesozoic. The strong crust–mantle interaction and magmatism in the northern margin of North China were derived from the earliest Mesozoic paleo-Asian Ocean, which closed due to the Mongolian continental block colliding with the northern margin of the North China Craton; then, the northern margin of North China entered the postorogenic extensional tectonic system [18–21]. Under this regime that was mainly characterized by extensional activity, fault zone activity continued to develop from the Early–Middle Jurassic to the Late Jurassic and provided favorable space for magma intrusion. Close to the Late Jurassic, the faults reactivated due to extensional activities, leading to the deposition of the Zhangjiakou volcanic rocks.

The magmatic activity in the Longhua area was multicyclic and formed a series of volcanic strata. According to eruption cycles and stratigraphic sequences, the volcanic strata are divided into the Zhangjiakou Formation and the Yixian Formation. The Zhangjiakou Formation is composed of $J_3z^2 \sim J_3z^4$ from bottom to top and mostly consists of volcanic and pyroclastic rocks. The pyroclastic

rocks of the Zhangjiakou Formation were dated to 135±1 Ma by zircon U-Pb ages [22]. The andesite is locally covered by volcanic rocks of the second member of the Zhangjiakou Formation. The Jurassic porphyry intrudes along an S–N-trending granite and andesitic stratum. The fourth member of the Zhangjiakou Formation mainly consists of rhyolitic tuff and locally trachytic breccia tuff. The Yixian Formation has an angular unconformity overlying the Zhangjiakou Formation and predominantly consists of pyroxene andesite, andesitic brecciated basalt, and rhyolitic tuff, reflecting the most extensive Mesozoic magmatism in the northern North China Craton. Early studies of fossils and isotope chronology of the Yixian Formation indicate that its age was approximately 122–129 Ma [23, 24].

The Longhua deposit occurs in the second member of the Zhangjiakou Formation, which contains tuff, rhyolitic ignimbrite, trachyandesite, and some conglomerate beds (Figure 1(b)). The chalcedony bodies of the Longhua deposit are hosted in rhyolitic ignimbrite in the Zhangjiakou Formation. Individual orebodies are several meters to more than 200 m in length and approximately 3–5 m in depth. The chalcedonies are long lenticular, vein, and/or irregular in shape (Figures 2(a) and 2(b)) and occur along the fragile fractures within the host rock.

Rhyolitic ignimbrite appears milky white to grayish purple and shows slight weathering. A certain chalcedony body is shaped as an irregular rack and may contain fragments of the host rocks. Its upper and lower parts may exhibit different features. The upper boundary of the upper parts is clear and often not fully occupied. In comparison, the lower part is occupied fully inside the crack. Apart from such a distinct occurrence of the Longhua chalcedony, various fine quartz veins (less than 0.5 cm thick) inside the rhyolitic ignimbrite are well developed (Figure 2(b)).

3. Materials and Methods

The samples for this study were collected from fresh surface exposures, and all chalcedony-bearing rocks are rhyolitic ignimbrite. The gemological reference data of chalcedonies were acquired at the School of Gemology of the China University of Geosciences, Beijing (CUGB). Nondestructive basic gemological tests conducted using a refractometer, a hydrostatic balance, a microhardness tester, and ultraviolet lamps were carried out on representative samples. Thermogravimetric analysis was conducted using a Shimadzu DTG-60, which was used to determine the weight changes. The sample was heated from room temperature to 1000°C at a constant rate of 5°C/min.

The texture of chalcedonies and the distribution of silica phases, especially the sequence of silica crystallization, were observed by polarized light microscopy and scanning electron microscopy (SEM) with a Superatm 55 at CUGB. Samples were prepared for SEM analysis by placing representative sample material onto a glass slide and then applying a platinum coating.

The chemical compositions of chalcedonies and rhyolitic ignimbrites were determined using a JXA-8230 electron microprobe equipped with four Wavelength Dispersive
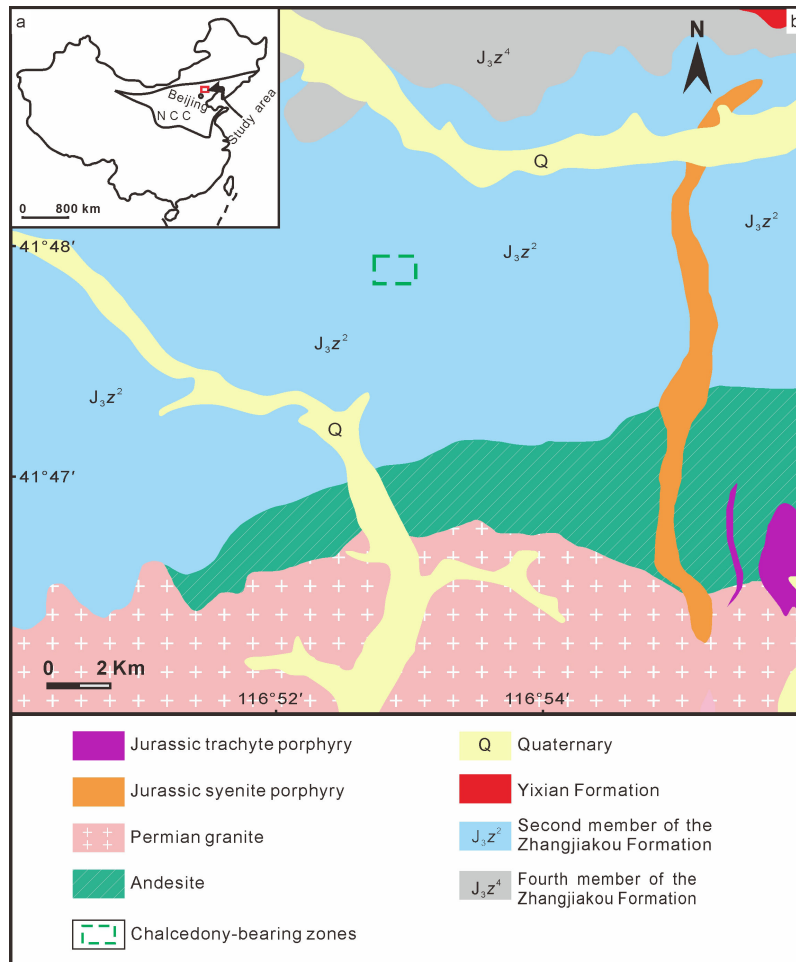
FIGURE 1: (a) Simplified tectonic map of China [51]. (b) Geological map of Longhua chalcedony deposit and its adjacent areas (modified after RGHPMI 1996).
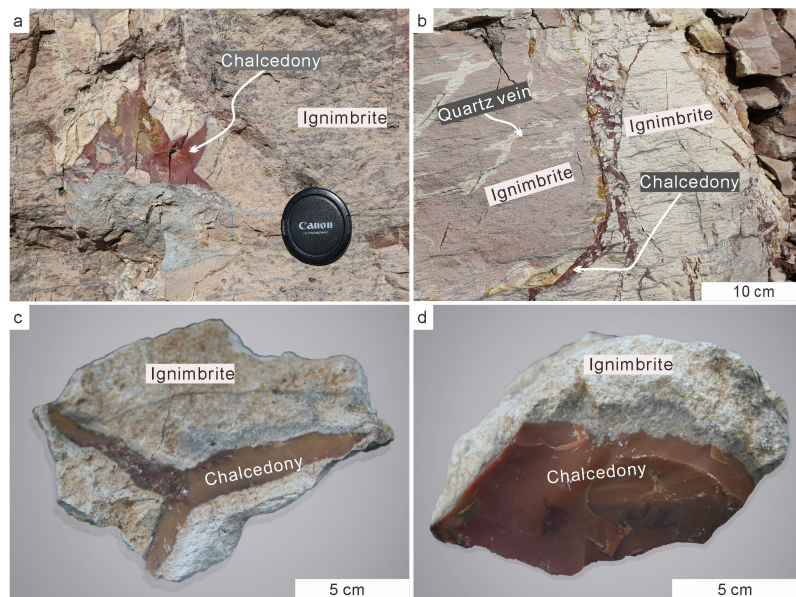

FIGURE 2: Field photographs showing (a) outcrop of irregular chalcedony. (b) Outcrop of chalcedony with many breccias, the lower fracture was fully filled by chalcedony, whereas chalcedony gradually decreased and finally vanished up to the upmost part. (c–d) Photographs of chalcedony-bearing rocks.

Spectrometer at the Institute of Mineral Resources of the Chinese Academy of Geological Sciences. The conditions were as follows: a spot size of 5 μm, an acceleration voltage of 15 kV, and a beam current of 20 nA. Matrix corrections were carried out using the ZAF correction program. Electron microprobe analysis (EMPA) standards include the following minerals: quartz for Si, anorthite for Ca and Al, albite for Na, K-feldspar for K, rutile for Ti, chromium oxide for Cr, tephroite for Mn, and biotite for Fe and Mg. All mineral formulas were recalculated by choosing a method based on the number of oxygen using GEOKIT software [25].

Oxygen isotope analyses were performed by the BrF_5 analytical method (MAT 253 EM) at the Institute of Mineral Resources of the Chinese Academy of Geological Sciences and calculated according to Vienna Standard Mean Ocean Water (V-SMOW). The analytical accuracies of the long-term standard measurements of $\delta^{18}O$ were ±0.2‰.

Samples with red inclusions were selected and analyzed by polarizing microscopic observations combined with Raman spectroscopy (Horiba LabRAM HR Evolution) at the School of Gemology, CUGB. The instrument was equipped with a Peltier-cooled charged-coupled device detector and edge filters, and the laser was a 532 nm Neodymium-YttriumAluminiumGarnet laser. The test coverage ranged from 200 to 2000 cm^{-1}, and the spectral resolution was ~1 cm^{-1}. The spectra were recorded at a laser power of 50 mW with a 3-second acquisition time. The curve fitting algorithm was used to fit the spectrum within the test range in OriginPro9 software. Based on previous work, the ratio of the area of the 501 and 464 cm^{-1} peaks can be used to identify the moganite contents [26].

The quartz crystallinity index (QCI) and microstructural analysis of chalcedony were acquired at the Beijing X-ray powder diffraction Laboratory, CUGB, using a Rigaku Smart Lab 9Kw target X-ray diffractometer. Selected samples were analyzed by X-ray powder diffraction and powdered to a particle size of 400 mesh. Samples of the chalcedony were orange–yellow, white, red, and dark yellow, and a standard QCI research sample was used. The standard sample was transparent, and colorless synthetic crystals had no impurity inclusions, that is, they were compliant with the internal standard as defined in the original paper [27]. The instrument was launched at 1.54059 Å for wavelength 1 and 1.54441 Å for wavelength 2 and operated at 40 kV and 200 mA. The initial and final wavelengths for the samples were performed at a scanning rate of 0.01°/s for 2θ from 66° to 70°. The algorithm for calculating the crystallinity of quartz was the five-finger diffraction peak near 68°. For microstructural analysis using diffraction profiles, from 15° to 70° 2θ at 0.02° 2θ increments with a 1-second counting time per increment, the standard sample was LaB6, and settings and operating conditions were as specified above.

4. Results

4.1. Petrography.
The rhyolitic ignimbrites are mainly grayish white to yellowish white, and all samples have a welded tuff texture and pseudoflowage structures with visible quartz veins and small pores (Figures 3(a) and 3(b)). The ignimbrites are several centimeters to 15 cm in length. Mineralogically, they consist of 50–70 vol.% sanidine (0.1–2 mm in size), 10–15 vol.% plagioclase (0.5–1 mm in size), 8–10 vol.% quartz (0.1–0.2 mm in size), 3–5 vol.% biotite (0.3–0.6 mm in size), and accessory minerals, such as Fe-Ti oxides, apatite, titanite, and zircon. The sanidines are subhedral to euhedral and have cleavage and cracking present on the surfaces. The feldspars have irregular shapes (Figure 3(c)). Polysynthetic twins are developed in plagioclase. The biotite occurs as plate-shaped or short columns with pronounced cleavage (Figure 3(d)). Sharp-angled or broken crystals and large amounts of semiplastic fragments are present in host rocks. Sharp triangular crystals and irregular feldspar (Figure 3(c)) reveal that mineral fragments within rocks and volcanic materials account for more than 90%.

4.2. Physical Properties.
The Longhua chalcedony samples are red, yellow, and white/colorless and display a vitreous luster in natural light and semitranslucent to translucent. The refractive index measured with the distant vision method was approximately 1.54 and displayed specific gravity (SG) values of 2.55 to 2.56 and H values of 6.07 to 6.34 (Table 1). These SG and H values were slightly lower than those of the typical chalcedony [28, 29]. The measured weight loss percentages of the samples were 2.18%, 1.97%, 2.32%, and 2.15% (Figure 4). These weight loss values were greater than those of other sedimentary chalcedonies, which contain less than 2% weight loss [4]. All the samples were inert to both short- and longwave UV. In addition, red inclusions were present in almost every red or yellow sample (Figures 2(c) and 2(d)).

4.3. Texture of the Chalcedony.
The images of the representative slice under polarized light showed the typical cryptocrystalline structure (Figure 5) with a sequence and optical continuity in the formation of the chalcedony, which is classified into three subsequences (S-I, S-II, and S-III). The external part of the chalcedony samples contained wall-lining layers of elongated prismatic macrocrystalline quartz, which had a comb-like appearance (S-I), reflecting vertical internal growth.

S-II displayed a thin layer of crystallites (i.e., transition phase), forming fan-like fiber bundles that radiated from points located on earlier layers and grew toward the central region. The color of this layer probably resulted from fine iron oxides and hydroxides scattered within the silica matrix. The fiber crystallites could be recognized optically only under crossed polarized light because this layer was very narrow, and the fibers were accompanied by conical extinction. S-III represents a relatively pure region, which mainly formed a uniform cryptocrystalline phase in the core and showed the last stage of growth within the whole chalcedony body. Within this domain, the structure of the cryptocrystalline phase was more delicate, and the extinction was almost invisible compared with previous reports for chalcedony from other localities.
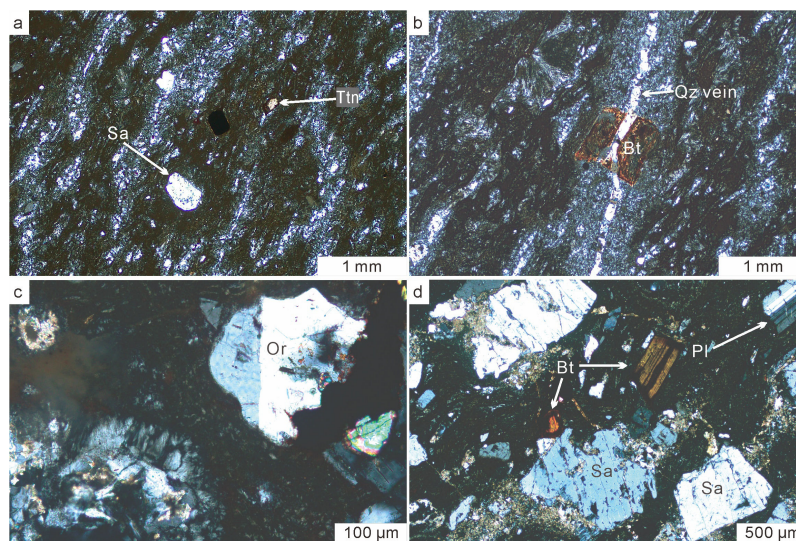
FIGURE 3: (a–b) Occurrence of sanidine, titanite, biotite, and quartz vein. (c) Occurrences of triangular crystal and orthoclase. (d) Occurrence of sanidine, biotite, and growth twins of plagioclase in ignimbrites. Mineral abbreviation: Sa, sanidine; Ttn, titanite; Qz, quartz; Or, orthoclase; Pl, plagioclase; Bt, biotite [52].

TABLE 1: Disceptions and physical measures of the studied Longhua chalcedony.

Sample	Color	Luster	Transparency	Refractive index	Specific gravity	Optical character	Hardness	UV fluorescence
LH-19	Red	Vitreous	Translucent	1.54	2.55	Anisotropic aggregate	6.31	Inert
LH-20	Red and orange-red	Vitreous	Translucent	1.54	2.55	Anisotropic aggregate	6.33	Inert
LH-22	Dark red	Vitreous	Translucent	1.54	2.55	Anisotropic aggregate	6.33	Inert
LH-25	Red	Vitreous	Translucent	1.54	2.55	Anisotropic aggregate	6.34	Inert
LH-42	Red and orange-red	Vitreous	Translucent	1.54	2.55	Anisotropic aggregate	6.33	Inert
LH-119	Dark red	Vitreous	Translucent	1.54	2.55	Anisotropic aggregate	6.33	Inert
LH-28	Yellow and orange yellow	Vitreous	Translucent	1.54	2.56	Anisotropic aggregate	6.07	Inert
LH-92	Yellow	Vitreous	Translucent	1.54	2.56	Anisotropic aggregate	6.08	Inert
LH-120	Deep yellow	Vitreous	Translucent	1.54	2.56	Anisotropic aggregate	6.07	Inert
LH-64	Grayish white	Vitreous	Semitranslucent	1.54	2.55	Anisotropic aggregate	6.33	Inert
LH-67	White	Vitreous	Translucent	1.54	2.55	Anisotropic aggregate	6.33	Inert
LH-71	Grayish white	Vitreous	Translucent	1.54	2.55	Anisotropic aggregate	6.33	Inert

The SEM images (Figure 6) revealed a variety of internal structures and the sequence of the silica phases from the rim to the center. SEM images of the chalcedony showed three internal growth subsequences of S-I, S-II, and S-III (Figure 6(a)), which is consistent with the observation under the polarizer. Our study determined that the Longhua chalcedonies consisted of silica platelets that were not of uniform diameter and had many pores. These platelets were in a disorderly arrangement and were typically cemented by sphere-like nanograins (Figures 6(c)
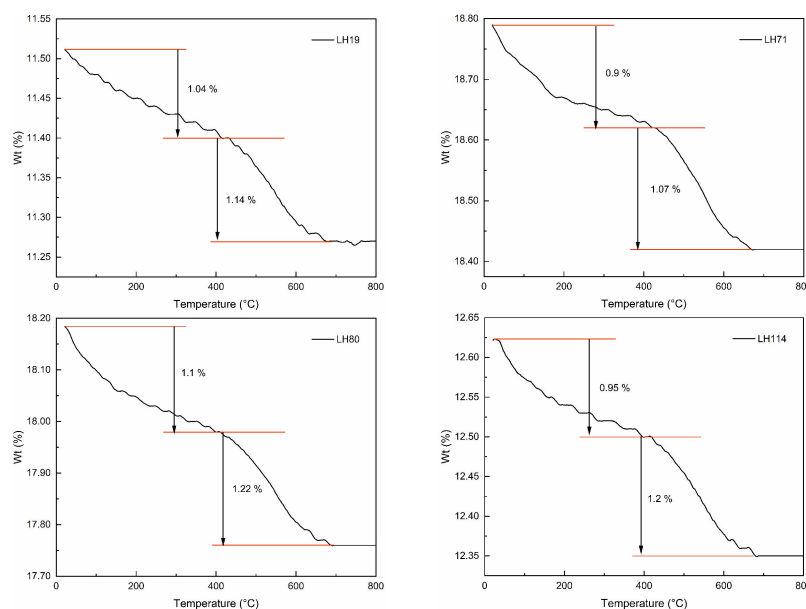
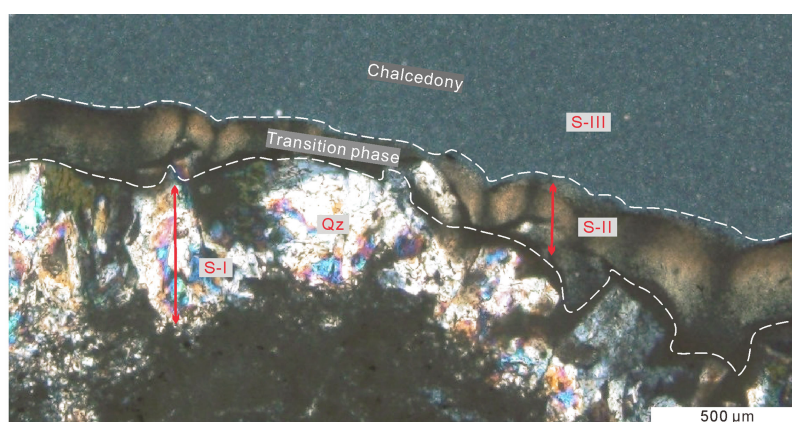FIGURE 4: Thermogravimetric analysis pattern of Longhua chalcedony.

FIGURE 5: Photomicrographs showing a formation sequence of chalcedony.

and 6(d)). It is noted that between S-II and S-III, a loose boundary with dense fine pores existed, which might be partially filled by secondary iron-rich materials, displaying a thin red-orange appearance.

4.4. Mineral Chemistry. Phenocryst minerals of the rhyolitic ignimbrite mainly included feldspar and biotite. Results of electron microprobe mineral analysis of alkaline feldspar from Longhua together with the calculated number of ions per unit cell show that they are mainly Ab and Or, with low An contents (Table 2). Alkaline feldspar that appears as phenocrysts has Or (40.18–55.55 mol%), Ab (40.22–57.71 mol%), and An (1.69–4.64 mol%).

The biotites were characterized by low SiO_2 and relatively high TiO_2. Si ranged from 2.85 to 2.91 a.p.f.u., Al^{iv} ranged from 1.10 to 1.15 a.p.f.u., Ti ranged from 0.12 to 0.17 a.p.f.u., Fe^{3+} ranged from 0.12 to 0.22 a.p.f.u., Fe^{2+} ranged from 0.66 to 0.94 a.p.f.u., Mn ranged from 0.01 to

0.02 a.p.f.u., and Mg ranged from 1.53 to 1.74 a.p.f.u. (Table 3).

4.5. Oxygen Isotopes. The $\delta^{18}O$ values of the low-crystallinity chalcedonies range between +15.2 and +15.8‰ (Table 4). According to the quartz–water curve of Matsuhisa and Goldsmith [30] and based on the equation $\Delta^{18}O = 1000 \ln\alpha QW = 3.34 \ (10^6 \ T^{-2}) - 3.31$ for equilibrium isotope exchange with meteoric water (−10‰), oceanic water (0‰), and magmatic water (+8‰), temperatures were calculated.

4.6. Spectroscopy Analysis. The Raman spectra (Figure 7 and Table 5) of different silica polymorphs measured from selected areas of the chalcedonies show that the primary bands at approximately 464 and 501 cm^{-1} were related to symmetric stretching–bending vibrations of α-quartz and moganite, respectively [26]. The Raman spectrum of the
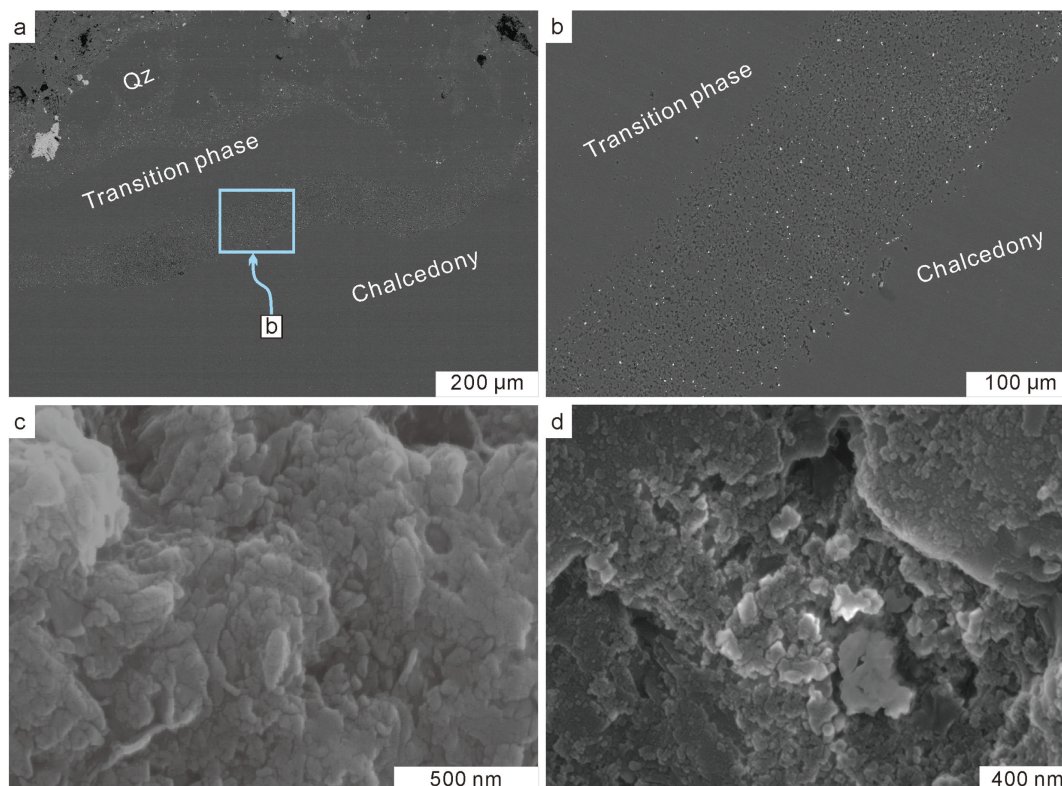
FIGURE 6: Scanning electron microscope images of the Longhua chalcedony: (a) showing growth subsequences from comb-like quartz layers (S-I), to transition phase layer (S-II), and uniform cryptocrystalline phase (S-III), (b) a close-up (blue rectangle in a) showing a loose boundary (with dense fine pores) between S-II and S-III, and (c–d) showing the microstructure of the silica platelets.

TABLE 2: Representative chemical compositions of the alkali feldspar in host rock.

Sample no.	LH118-4	LH118-5	LH118-7	LH118-14	LH71-1	LH71-2	LH71-3	LH06-1
Na_2O	4.73	4.85	3.80	5.41	5.94	6.13	6.54	5.69
Al_2O_3	19.6	19.14	20.58	19.97	20.72	20.50	20.51	20.12
K_2O	9.05	9.42	7.97	9.09	7.51	7.57	6.92	8.23
CaO	0.94	0.67	0.72	0.41	0.34	0.40	0.43	0.40
FeO	0.06	0.17	0.20	0.16	0.13	0.18	0.18	0.18
SiO_2	64.15	64.97	65.94	64.20	65.13	64.88	64.57	64.81
BaO	1.45	0.69	0.68	0.09	0.00	0.01	0.12	0.00
Total	99.98	99.91	99.89	99.33	99.77	99.67	99.27	99.43
Si	2.94	2.96	2.96	2.93	2.93	2.93	2.92	2.94
Al	1.06	1.03	1.09	1.08	1.10	1.09	1.10	1.08
Fe2	0.00	0.01	0.01	0.01	0.00	0.01	0.01	0.01
Ca	0.05	0.03	0.04	0.02	0.02	0.02	0.02	0.02
Na	0.42	0.43	0.33	0.48	0.52	0.54	0.57	0.50
K	0.53	0.55	0.46	0.53	0.43	0.44	0.40	0.48
Ba	0.05	0.03	0.02	<0.01	0.00	<0.01	<0.01	0.00
Or	53.15	54.27	55.55	51.47	44.66	43.96	40.18	47.82
An	4.64	3.25	4.22	1.96	1.69	1.97	2.11	1.95
Ab	42.21	42.48	40.22	46.57	53.65	54.07	57.71	50.24

macrocrystalline quartz layer revealed only the presence of α-quartz, whereas the content of moganite varied from the fiber crystallite layer to the main cryptocrystalline chalcedony. The α-quartz seemed to dominate over the

TABLE 3: Representative chemical compositions of the biotite in host rock.

Sample no.	LH118-1	LH118-3	LH118-8	LH118-10	LH118-13
SiO_2	38.97	39.29	38.03	38.91	38.76
TiO_2	3.07	2.85	2.69	2.06	3.02
Al_2O_3	14.40	14.08	13.66	12.69	14.29
FeO_t	14.17	14.27	15.54	16.88	16.19
MnO	0.15	0.17	0.18	0.37	0.10
MgO	15.17	15.18	15.58	15.61	13.77
CaO	0.01	0.00	0.02	0.00	0.00
Na_2O	0.62	0.59	0.44	0.48	0.47
K_2O	8.84	9.28	8.86	9.07	9.06
Cl	0.04	0.05	0.04	0.07	0.05
Cr_2O_3	0.04	0.00	0.01	0.01	0.01
NiO	0.00	0.00	0.00	0.04	0.00
BaO	0.84	0.36	0.19	0.00	0.72
Total	96.32	96.12	95.24	96.19	96.44
Si	2.88	2.90	2.85	2.91	2.89
Al^{iv}	1.12	1.10	1.15	1.10	1.12
Al^{vi}	0.13	0.13	0.06	0.02	0.14
Ti	0.17	0.16	0.15	0.12	0.17
Fe^{3+}	0.22	0.20	0.15	0.12	0.22
Fe^{2+}	0.66	0.69	0.82	0.94	0.79
Mn	0.01	0.01	0.01	0.02	0.01
Mg	1.67	1.67	1.74	1.74	1.53
Ca	<0.01	0.00	<0.01	0.00	0.00
Na	0.09	0.08	0.06	0.07	0.07
K	0.83	0.87	0.85	0.86	0.86
Cl	0.01	0.01	0.01	0.01	0.01
Cr	<0.01	0.00	<0.01	<0.01	<0.01
Ni	0.00	0.00	0.00	<0.01	0.00
Ba	0.02	0.01	0.01	0.00	0.02
Total	7.81	7.83	7.86	7.91	7.83

Note: FeO_t—total iron; Al^{iv}—tetrahedral Al; Al^{vi}—octahedral Al.

TABLE 4: Oxygen isotope compositions ($\delta^{18}O_{VSMOW}$) of investigated samples.

Sample	$\delta^{18}O_{VSMOW}$ [‰]	T_{met}(°C)	T_{oc}(°C)	T_{mag}(°C)
LH-19	15.2	69	152	291
LH-71	15.8	66	145	275
LH-92	15.6	67	147	280
LH-20	15.7	66	146	278

moganite, which occurred in the core regions of the chalcedony. Raman band integral ratios for that moganite content as derived were calculated using the methods of Götze, Nasdala [26]. The premise is that "moganite + quartz = 100%," which may actually contain a small
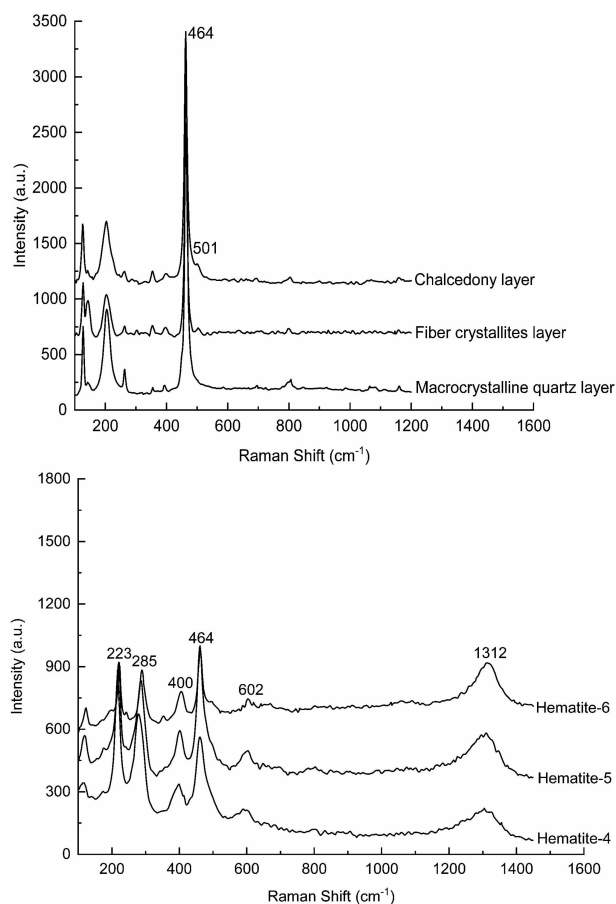

FIGURE 7: Raman spectra collected from various portions of Longhua chalcedony demonstrated the presence of moganite and α-quartz with (points 4–6) hematite inclusions.

amount of water [31]. The results revealed that the contents of moganite in the fiber crystallite layer and the main cryptocrystalline chalcedony were approximately 38% and 28%, respectively.

Interesting accumulations of red inclusions (Figure 7) were identified with Raman spectroscopy as hematites [32, 33], with points 4–6 having similar spectra and characteristic bands at 223, 285, 400, 464, 602, and 1312 cm⁻¹. These bands are attributed to symmetric bending vibrations of Fe–O [34]. All of these features are consistent with previous reports for iron oxides and hydroxides [35].

4.7. QCI and Microstructural Analysis. The QCI and microstructural analysis of grain size were measured to estimate the formation temperature of chalcedony. The QCI, as determined on the four chalcedonies, as well as standard quartz (Figure 8), was calculated according to the equation CI = 10·F·a/b [27, 36]. Examples of partial X-ray diffraction (XRD) diffractograms show the quintuplet at approximately 67.62° 2θ. It is worth noting that the XRD pattern of LH119 is broader and diffuse, and the peak is visible only as a shoulder rather than a separate peak at 68.17° 2θ. In contrast, as the QCI increases, the peaks become better defined (steeper slopes and a narrower base)

Table 5: Raman band positions (cm⁻¹) and assignments of chalcedony from Longhua.

Point1: α-quartz	Point2: α-quartz +moganite	Point3: α-quartz +moganite	Mode symmetry
127	127	126	$E_{(LO+TO)}$
	142		
204	204	203	A1
262	262	262	$E_{(LO+TO)}$
354	353	354	A1
392	396	397	$E_{(TO)}$
464	464	462	A1
	501	500	A1
	798		$E_{(TO)}$
805		801	$E_{(LO)}$

Notes: Band assignments from Götze et al. [26].

and higher relative to the background [37]. Thus, the peak height for the reference standard quartz with an attributed QCI = 10 at up to 12,000 cps is nearly 1.5 times higher than that for the quartz in LH119 with a QCI = 1.3 at approximately 8000 cps.

The data obtained by XRD analysis were matched with the values of ideal quartz by using the comparative matching technique. The ideal XRD data were from the American Mineralogist Crystal Structure Database (AMCSD, cif reference code 0000789). The results revealed that the d-spacings of these samples are 3.35, 4.26, and 1.82, which correspond to the standard quartz based on the position of the relative intensity peak (I/Io) ≥ 5%.

The grain size was estimated using the Scherrer equation $D = \frac{0.94\lambda}{\beta cos\theta}$. The average grain sizes of the chalcedony samples are 54, 52, 42, and 51 nm. The results revealed that the grain size decreases as the diffraction line broadens, which is in agreement with data for the quintuplet peak above. The GSAS software used the standard card, 16331-ICSD SiO_2, and yielded the lattice constants of four representative chalcedony samples: a: 4.923, b: 4.923, and c: 5.416 Å; a: 4.921, b: 4.921, and c: 5.414 Å; a: 4.925, b: 4.925, and c: 5.418 Å; a: 4.921, b: 4.921, and c: 5.414 Å, respectively. The crystalline phases are trigonal within spacing group P3221.

5. Discussion

5.1. Rare Occurrence of Chalcedony.
Chalcedony, in general, has been reported to occur in carbonate, basalt, or sandstone [6, 38]. Occurring in rhyolitic ignimbrite, the Longhua chalcedony is excluded as the general type and recognized as a rare type.

Despite variations in mineral and chemical compositions, the chalcedony-bearing rocks from Longhua point to the pyroclastic formation of acidic ignimbrite (Figure 3). Three end-members of feldspars (40.18%–55.55% Or, 40.22%–57.71% Ab, and 1.69%–4.64% An) yield the

chemical formula $An_{2-5}Ab_{40-58}Or_{40-56}$ and are sanidine according to the classification diagram (Figures 9(a) and 9(b)).

Previous studies have demonstrated that mica compositions are related to the crystallization of magma or hydrothermal processes [39] and that magmatic types have higher TiO_2 and K_2O and lower Al_2O_3 contents [40]. Magnesian biotite in our samples from magmatic-type domains has a low level of Al_2O_3 and forms from a crust–mantle source with hybrid characteristics (Figure 9(c)), which is consistent with the strong crust–mantle interaction. This kind of magmatism occurs extensively along the tectonic system of Jurassic extensional fractures on the northern margin of the North China Craton.

Several agate deposits occur on the northern margin of the North China Craton, including the Xuanhua, Fuxin, and Alashan Agates. The Xuanhua Agate is a kind of microcrystalline variety of silica that occurs in trachyte [41], the Fuxin Agate occurs in basalt and/or andesite [42], and the Alashan Agate is abundant, has varieties, and occurs in basalt [43]. These agates share similarities both in their phases and their host rocks. However, the Longhua SiO_2 phase (chalcedony) is different from both the in-phase and host rocks.

This growth structure differs from the concentric structure of the agate cross-section. Agate in most cases started as cryptocrystalline or microcrystalline, after which it transitioned to fibrous chalcedony, then transitioned to macrocrystalline quartz or cavity types [44], indicating that the growth structure is contrary to that of Longhua chalcedony. Previous studies have suggested that the crystallization rate and stepwise self-organization of SiO_2 are the most important processes in the formation of the agate microstructure [12]. Thus, the structural disparities reveal that the crystallization modes of agate and the Longhua chalcedony are diverse.

Field and petrographic observations reveal that the Longhua chalcedony is a filling precipitation product of a kind of silica-rich fluid along fractures inside the rhyolitic ignimbrite. The fragile, distinct, flat, sharp profile of the fracture (Figure 2) obviously reflects its own generation by exotic tectonic stress after cooling consolidation instead of the deviation of intrinsic contraction after the cooling of the volcanic rhyolitic ignimbrite rock. This generation explains why the chalcedony occurred as long lenticular veins or irregular but not rounded bodies, as it was shaped after the outline of the fracture, which shows a large difference from the rounded, cavity-shaped outline of most of the agate bodies generated by intrinsic cooling contraction [45, 46]. This distinct occurrence in the chalcedony from Longhua manifests as a fingerprint characteristic among agate and other chalcedony deposits.

5.2. Temperature Estimation of Chalcedony Formation.
Oxygen isotope data have revealed that the temperatures of formation for the low-crystallinity chalcedony were between 66°C and 291°C. These temperatures cover a broad range between hydrothermal origins and sedimentary formations. However, we conclude from our oxygen isotope data and field observations that the low-crystallinity
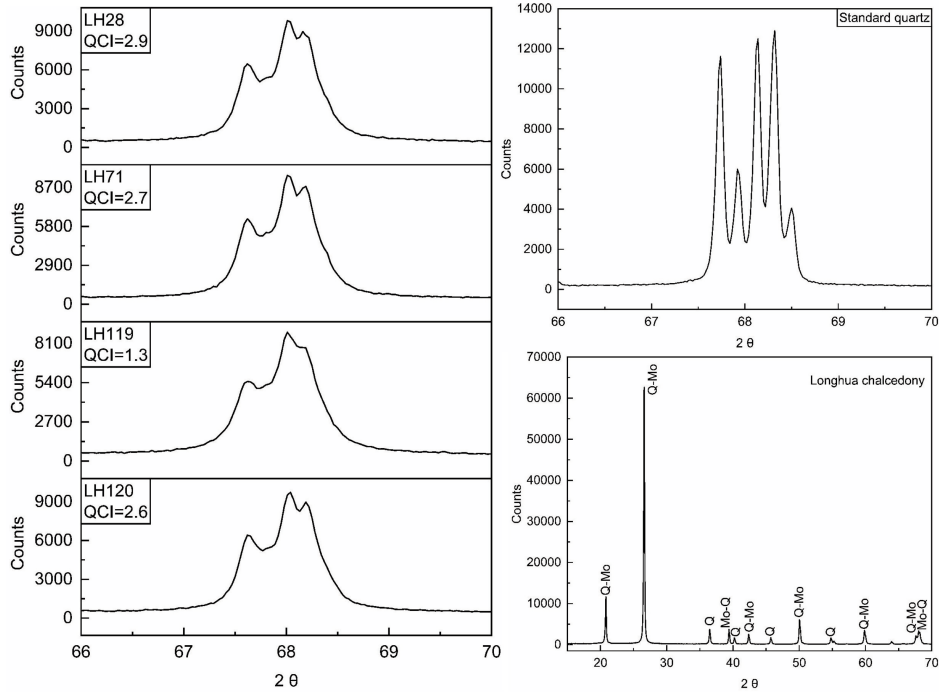
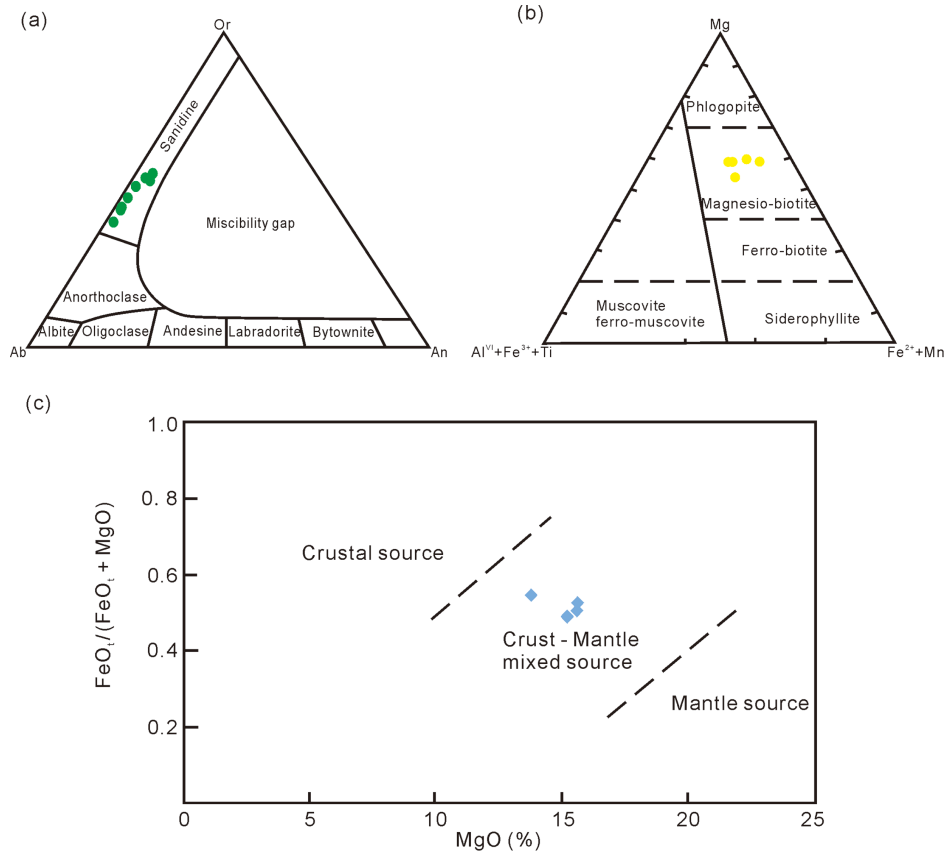FIGURE 8: Partial diffractograms of the Longhua chalcedony. Q, α-quartz; Mo, moganite.

FIGURE 9: (a) Ab-Or-An ternary diagram [53], (b) classification diagram of biotite [54], and (c) $FeO_t/(FeO_t + MgO)$ – MgO sources discriminating diagram for biotites [55].

chalcedony formed at modest temperatures of approximately 66°C. Different features between the upper and lower chalcedony within the fractures in the country rock, together with the open system of the fragile fractures, imply that fluid forming in the Longhua chalcedony was at a low temperature of less than 100°C. The upper and lower parts of the chalcedony-filling fractures in the host rock are different; in the upper part, chalcedony even vanishes (Figure 2(b)), indicating that the chalcedony grew from bottom to top, and hence, the chalcedony-forming fluids in the fracture cavity were clearly controlled under the gravity of the Earth. As the fracture was fragile and well developed, the system of the fractures hosting the chalcedony could be regarded as open to the fluid; thus, the fluid was approximated at one-atmosphere pressure. Assuming that the temperature of the fluid was higher than 100°C, water in the fluid would have evaporated to form a gas phase, caused a vapor crystallization layer beyond gravity and then formed concentric layers, such as agate, that grew from the outside to the center.

The very low degree of crystallinity and small crystal grains also imply that Longhua chalcedony formed at a very low temperature of less than 100°C. XRD analyses show that chalcedony has a very low degree of crystallinity (~1–3). The average grain size is ~50 nm, which indicates that this chalcedony has a tendency toward opal. The silica platelets in Longhua chalcedony are several orders of magnitude smaller than those in other regions of chalcedony. The shape of the nanograins is very similar to that of opal, and the grain size is similar to that of opal [47].

The tiny aggregates of hematite inclusions in the chalcedony are disorderedly distributed in the silica matrix, further showing that the formation temperature was less than 100°C and was most likely 40°C–80°C. Previous research has shown that ferruginous inclusions in chalcedony are mainly hematite or a mixture of hematite and goethite, and the coexistence of hematite and goethite is relatively stable at 40°C–80°C [6, 38].

5.3. Microstructure and Formation Mechanism of the Chalcedony. Growth structures of the Longhua chalcedony show that crystallization of lower parts in the fractures proceeded inward to the centers. In the final stage of its growth, a relatively uniform cryptocrystalline phase with a lower degree of crystallinity appeared. This phase differs from thin fiber crystallite layers with orange or red chalcedony in this deposit, although the fibers are much shorter than those in normal chalcedony and agate. We propose that this phase was transitional between opal and chalcedony, that is, the phase might be referred to as low-crystallinity chalcedony.

It is not difficult to distinguish between typical chalcedony and opal; however, an intermediate transitional phase naturally exists between chalcedony and opal. Such an intermediate transitional phase would have both transitional physical properties and microstructural characteristics in the range between chalcedony and opal. The relatively uniform cryptocrystalline phase of the Longhua chalcedony shows an apparent transition to opal. The SG and H values of all tested samples are generally below the

ranges of the most known chalcedony. These samples are closer to opal if assessed by microstructural features and a lower degree of crystallinity.

Most previous structural studies of common chalcedony have suggested that they are primary built blocks of platelets without cemented grains, which are not well stacked in order [3]. The microstructure of opal is mainly constructed of spheres or tablets, which are typically cemented by nanograins containing many pores from earlier studies [48]. However, SEM imaging of the Longhua chalcedony indicated that a large number of nanograins irregularly coalesced to build platelet-like structures with many pores. Such a structure is more similar to opal.

Chalcedonies from Longhua contain thin fiber crystallite layers with orange or red colors, which are associated with Fe compounds. This kind of radial fiber structure also appears in agate. Agate has periodic microscopic oscillation bands, whereas the fibers in agate are much longer than those in our specimens. This thin layer may be attributed to the space and crystallization rate in its formation. Accordingly, spiral growth theory could explain the fiber structure of chalcedony [49]. Rapid crystallization could lead to frequent errors in the bonding of silica monomers and tetrahedral chains. The Longhua chalcedony lacks periodic oscillation bands, and the fan-shaped fiber bands are very narrow, which likely results from lattice defects or trace element concentrations.

The existence of this stratification might indicate a decrease in the crystallinity of chalcedony from the outer part to the core. It is also related to the increase in the silica concentration in the ore-forming fluid [50]. This growth mechanism reveals the continuous penetration of silica-rich fluids, indicating that silica-rich fluids had complex fluctuations in physical and chemical conditions. Therefore, the macrocrystalline quartz layer has adequate silica concentration and a comb shape. The increase in the silica concentration in the crystallization medium then causes the formation of the cryptocrystalline phase. The results indicate that the structural evaluation is closely related to the maturity of the ore-forming fluid.

5.4. Gemological Applications. The red, yellow, and white/colorless uniform phases of Longhua chalcedony make them attractive forms of chalcedony. Some varieties exhibit a mixture of two colors or only a single color occupying the entire view. Their rich colors can provide analytical data for scientific color grading and additional applications of natural chalcedony and agate. Most carved pieces with a homogeneous, pure color and/or dendritic hematite display changeable and charming patterns. Among them, the chalcedony reminiscent of Chinese fairy tales is the most favorable in jade markets (Figure 10). The fine, homogeneous, and cryptocrystalline nature of the Longhua chalcedonies make them durable, which is the most recommended by jade carvers and traders.

In recent years, there is a higher demand for chalcedonies than resource supply. High-quality chalcedony like that from Longhua just meets the demand from the jewelry market. The chalcedony could also be a nice carving

Figure 10: Charming and ornately carved patterns of the Longhua-type chalcedony.

material, making it be qualified for almost any jewelry or object. The uniform phase with a lower degree of crystallinity, which is closer to opal in the point of the microstructure, marking it a potential application perspective. Consequently, the commercial value of such a uniform phase is expected to be higher than those of similar silica varieties in this way, and a determination of similar varieties is then necessary, which may have further clues for laboratory synthesis.

6. Implications

Typical chalcedonies have been reported to occur in carbonate, basalt, or sandstone [6, 38]. Our studies confirm that a novel type of chalcedony occurs in rhyolitic ignimbrite, with a rare occurrence and microstructure. The Longhua chalcedony, therefore, has a manifested fingerprint that is characteristic among agate and other chalcedonies. It exhibits long lenticular veins or irregular bodies, which show a distinct difference from the common chalcedonies and agate bodies.

We suggest that there is an intermediate transitional phase between typical chalcedony and opal, which should be considered as low-crystallinity chalcedony. Such an occurrence type of chalcedony could have valuable clues for searching for the same and the other silica varieties resource. Along with its economic value, our data would play an important role in mineralogy, especially in the exploration for similar chalcedony variety and resource prospecting.

Data Availability

All data supporting the results can be found in the manuscript.

Conflicts of Interest

The authors declare that they have no conflicts of interest.

References

[1] O. W. Flörke, H. Graetsch, B. Martin, K. Röller, and R. Wirth, "Nomenclature of Micro- and non-crystalline silica minerals, based on structure and Microstructure," *Neues Jahrbuch Für Mineralogie-Abhandlungen*, vol. 163, no. 1, pp. 19–42, 1991.

[2] V. Y. Prokofiev, V. S. Kamenetsky, S. L. Selektor, T. Rodemann, V. A. Kovalenker, and S. Z. Vatsadze, "First direct evidence for natural occurrence of colloidal silica in chalcedony-hosted Vacuoles and implications for ore-forming processes," *Geology*, vol. 45, no. 1, pp. 71–74, 2017.

[3] M. Hatipoğlu, S. C. Chamberlain, and Y. Kibici, "Characterization of the Sündikendağı deposit of moganite-rich, blue

chalcedony nodules, Mayıslar–Sarıcakaya (Eskişehir), Turkey," *Ore Geology Reviews*, vol. 54, October, pp. 127–137, 2013.

[4] M. Hatipoğlu, Y. Tuncer, R. Kibar, A. Çetin, T. Karalı, and N. Can, "Thermal properties of gem-quality moganite-rich blue chalcedony," *Physica B*, vol. 405, no. 22, pp. 4627–4633, 2010.

[5] Y. M. Xia, S. L. Dai, D. P. Chen, et al., "Gemological classification and identification characteristic of agate," *Mineralogy and Petrology*, vol. 40, no. 2, pp. 1–14, 2020.

[6] J. Götze, R. Möckel, U. Kempe, I. Kapitonov, and T. Vennemann, "Characteristics and origin of agates in sedimentary rocks from the Dryhead area, Montana, USA," *Mineralogical Magazine*, vol. 73, no. 4, pp. 673–690, 2009.

[7] T. Moxon, D. R. Nelson, and M. Zhang, "Agate Recrystallisation: Evidence from samples found in Archaean and Proterozoic host rocks, Western Australia," *Australian Journal of Earth Sciences*, vol. 53, no. 2, pp. 235–248, 2006.

[8] T. Moxon and S. J. B. Reed, "Agate and chalcedony from igneous and sedimentary hosts aged from 13 to 3480 ma: a Cathodoluminescence study," *Mineralogical Magazine*, vol. 70, no. 5, pp. 485–498, 2006.

[9] G. Parthasarathy, A. C. Kunwar, and R. Srinivasan, "Occurrence of moganite-rich chalcedony in Deccan flood basalts, Killari, Maharashtra, India," *European Journal of Mineralogy*, vol. 13, no. 1, pp. 127–134, 2001.

[10] T. Moxon, S. J. B. Reed, and M. Zhang, "Metamorphic effects on agate found near the Shap granite, Cumbria, England: as demonstrated by petrography, X-ray diffraction and spectroscopic methods," *Mineralogical Magazine*, vol. 71, no. 4, pp. 461–476, 2007.

[11] J. P. Pretola, "A feasibility study using silica Polymorph ratios for Sourcing Chert and chalcedony Lithic materials," *Journal of Archaeological Science*, vol. 28, no. 7, pp. 721–739, 2001.

[12] J. Götze, R. Möckel, T. Vennemann, and A. Müller, "Origin and geochemistry of agates in Permian volcanic rocks of the Sub-Erzgebirge basin, Saxony (Germany)," *Chemical Geology*, vol. 428, June, pp. 77–91, 2016.

[13] E. Gliozzo, B. Cairncross, and T. Vennemann, "A geochemical and micro-textural comparison of basalt-hosted chalcedony from the Jurassic Drakensberg and Neoarchean Ventersdorp Supergroup (Vaal River alluvial gravels), South Africa," *International Journal of Earth Sciences*, vol. 108, no. 6, pp. 1857–1877, 2019.

[14] J. Götze, H. Berek, and K. Schäfer, "Micro-structural phenomena in agate/chalcedony: Spiral growth," *Mineralogical Magazine*, vol. 83, no. 02, pp. 281–291, 2019.

[15] M. Ye and A. H. Shen, "Gemmological and mineralogical characteristics of Chrysocolla chalcedony from Taiwan, Indonesia and the USA, and their separation," *The Journal of Gemmology*, vol. 37, no. 3, pp. 262–280, 2020. http://www.gem-a.com/publications/journal-of-gemmology.aspx.

[16] D. B. Mao, C. T. Zhong, F. Q. Zhao, Z. H. Chen, Y. C. Zuo, and X. D. Hu, "Geochronology and geochemistry of the Mesozoic volcanic-Subvolcanic rocks in West Longhua area, northern Hebei province," *Geochimica*, vol. 34, no. 6, pp. 574–586, 2005.

[17] H. C. Xu, Y. P. Guo, X. Peng, and H. P. Zhao, "Relationship between the Mesozoic Intrusives and Yanshan Orogenic process in the Weichang-Longhua belt, Hebei province," *Geological Survey and Research*, vol. 30, no. 1, pp. 1–12, 2007.

[18] W. J. Xiao, B. F. Windley, J. Hao, and M. G. Zhai, "Accretion leading to collision and the Permian Solonker Suture, inner Mongolia, China: termination of the central Asian Orogenic belt," *Tectonics*, vol. 22, no. 6, pp. 1–20, 2003.

[19] Y. Zhao, G. Xu, S. H. Zhang, et al., "Yanshanian movement and conversion of Tectonic regimes in East Asia," *Earth Science Frontiers*, vol. 11, no. 3, pp. 319–328, 2004.

[20] B. Chen, B. M. Jahn, and W. Tian , "Evolution of the Solonker Suture zone: constraints from zircon U–Pb ages, Hf isotopic ratios and whole-rock Nd–Sr Isotope compositions of subduction- and collision-related magmas and forearc sediments," *Journal of Asian Earth Sciences*, vol. 34, no. 3, pp. 245–257, 2009.

[21] C. H. Zhang, H. L. Deng, C. M. Li, Z. Lu, and H. D. Deng, "An out-of-syncline thrust model for the "Chengde thrust sheet" in central intraplate Yanshan Orogenic belt, northern North China Craton," *Earth Science Frontiers*, vol. 19, no. 5, pp. 27–40, 2012.

[22] H. H. Wei, Q. R. Meng, G. L. Wu, and L. Li, "Multiple controls on rift basin sedimentation in volcanic settings: insights from the anatomy of a small early Cretaceous basin in the Yanshan belt, northern North China," *Geological Society of America Bulletin*, vol. 124, nos. 3–4, pp. 380–399, 2012.

[23] K. Q. Gao, J. Y. Chen, J. Jia, and J. Gardner, "Taxonomic diversity, stratigraphic range, and exceptional preservation of Juro-Cretaceous salamanders from northern China," *Canadian Journal of Earth Sciences*, vol. 50, no. 3, pp. 255–267, 2013.

[24] Y. Xu and H. Zhang, "Secular evolution of the Lithospheric mantle beneath the northern margin of the North China Craton: Insights from zoned Olivine xenocrysts in early Cretaceous basalts," *GSA Bulletin*, vol. 132, nos. 11–12, pp. 2353–2366, 2020.

[25] Y. F. Lu, "Geokit-A geochemical toolkit for Microsoft Excel," *Geochimica*, vol. 33, no. 5, pp. 459–464, 2004.

[26] J. Götze, L. Nasdala, R. Kleeberg, and M. Wenzel, "Occurrence and distribution of "moganite" in agate/chalcedony: a combined micro-Raman, Rietveld, and Cathodoluminescence study," *Contributions to Mineralogy and Petrology*, vol. 133, nos. 1–2, pp. 96–105, 1998.

[27] K. J. Murata and M. B. Norman, "An index of Crystallinity for quartz," *American Journal of Science*, vol. 276, no. 9, pp. 1120–1130, 1976.

[28] C. Frondel, "Characters of quartz fibers," *American Mineralogist*, vol. 63, nos. 1–2, pp. 17–27, 1978.

[29] J. E. Shigley, B. M. Laurs, and N. D. Renfro, "Chrysoprase and Prase opal from Haneti, central Tanzania," *Gems & Gemology*, vol. 45, no. 4, pp. 271–279, 2009.

[30] Y. Matsuhisa, J. R. Goldsmith, and R. N. Clayton, "Oxygen isotopic fractionation in the system quartz-albite-anorthite-water," *Geochimica et Cosmochimica Acta*, vol. 43, no. 7, pp. 1131–1140, 1979.

[31] C. Hardgrove and A. D. Rogers, "Thermal infrared and Raman microspectroscopy of moganite-bearing rocks," *American Mineralogist*, vol. 98, no. 1, pp. 78–84, 2013.

[32] A. M. Jubb and H. C. Allen, "Vibrational spectroscopic characterization of hematite, maghemite, and magnetite thin films produced by vapor deposition," *ACS Applied Materials & Interfaces*, vol. 2, no. 10, pp. 2804–2812, 2010.

[33] D. Bersani, P. P. Lottici, and A. Montenero, "Micro-Raman investigation of iron oxide films and powders produced by sol–gel syntheses," *Journal of Raman Spectroscopy*, vol. 30, no. 5, pp. 355–360, 1999. http://doi.wiley.com/10.1002/(SICI)1097-4555(199905)30:5<>1.0.CO;2-G.

[34] M. A. Legodi and D. Dewaal, "The preparation of magnetite, goethite, hematite and maghemite of pigment quality from mill scale iron waste," *Dyes and Pigments*, vol. 74, no. 1, pp. 161–168, 2007.

[35] D. L. A. de Faria, S. Venâncio Silva, and M. T. de Oliveira, "Raman Microspectroscopy of some iron oxides and oxyhydroxides," *Journal of Raman Spectroscopy*, vol. 28, no. 11, pp. 873–878, 1997. http://doi.wiley.com/10.1002/(SICI)1097-4555(199711)28:11<>1.0.CO;2-L.

[36] M. Y. He and P. Wang, "The Crystallinity of quartz and its Typomorphic significance," *Mineralogy and Petrology*, vol. 14, no. 3, pp. 22–28, 1994.

[37] N. Marinoni and M. A. T. M. Broekmans, "Microstructure of selected aggregate quartz by XRD, and a critical review of the Crystallinity index," *Cement and Concrete Research*, vol. 54, December, pp. 215–225, 2013.

[38] M. Dumańska-Słowik, T. Powolny, M. Sikorska-Jaworowska, A. Gaweł, L. Kogut, and K. Poloński, "Characteristics and origin of agates from Płóczki Górne (lower Silesia, Poland): A combined microscopic, micro-Raman, and Cathodoluminescence study," *Spectrochimica Acta. Part A, Molecular and Biomolecular Spectroscopy*, vol. 192, pp. 6–15, 2018.

[39] S. Z. Afshooni, H. Mirnejad, D. Esmaeily, and H. A. Haroni, "Mineral chemistry of hydrothermal biotite from the Kahang porphyry copper deposit (NE Isfahan), central province of Iran," *Ore Geology Reviews*, vol. 54, October, pp. 214–232, 2013.

[40] A. Parsapoor, M. Khalili, F. Tepley, and M. Maghami, "Mineral chemistry and isotopic composition of magmatic, re-equilibrated and hydrothermal biotites from Darreh-Zar porphyry copper deposit, Kerman (southeast of Iran)," *Ore Geology Reviews*, vol. 66, April, pp. 200–218, 2015.

[41] D. Y. Zhou, G. H. Shi, S. Z. Liu, and B. L. Wu, "Mineralogy and magnetic behavior of yellow to red Xuanhua-type agate and its indication to the forming condition," *Minerals*, vol. 11, no. 8, p. 877, 2021.

[42] Y. L. Wang, M. S. Zhong, C. Jia, et al., "Metallogenic regularity and prospecting orientation of agate in volcanic rocks of Fuxin area, western Liaoning," *Geology of China*, vol. 38, no. 5, pp. 1179–1187, 2011.

[43] H. F. Li, "Geological characteristics and value of agate in inner Mongolia," *Jewelry*, vol. 5, no. 2, pp. 47–49, 1991.

[44] T. Powolny, M. Dumańska-Słowik, M. Sikorska-Jaworowska, and M. Wójcik-Bania, "Agate mineralization in spilitized Permian volcanics from "Borówno" quarry (lower Silesia, Poland) – microtextural, mineralogical, and geochemical constraints," *Ore Geology Reviews*, vol. 114, November, p. 103130, 2019.

[45] P. J. Heaney and A. M. Davis, "Observation and origin of self-organized textures in agates," *Science (New York, N.Y.)*, vol. 269, no. 5230, pp. 1562–1565, 1995.

[46] T. Moxon, C. M. Petrone, and S. J. B. Reed, "Characterization and genesis of horizontal banding in Brazilian agate: An X-ray diffraction, Thermogravimetric and electron Microprobe study," *Mineralogical Magazine*, vol. 77, no. 3, pp. 227–248, 2013.

[47] M. Hatipoğlu, "The Nano-grain sizes of the Opaline matrix components in Anatolian fire Opals," *Journal of Non-Crystalline Solids*, vol. 356, nos. 28–30, pp. 1408–1415, 2010.

[48] E. Gaillou, E. Fritsch, B. Aguilar-Reyes, et al., "Common gem opal: An investigation of micro- to nano-structure," *American Mineralogist*, vol. 93, nos. 11–12, pp. 1865–1873, 2008.

[49] P. J. Heaney, "A proposed mechanism for the growth of chalcedony," *Contributions to Mineralogy and Petrology*, vol. 115, no. 1, pp. 66–74, 1993.

[50] M. W. French, R. H. Worden, and D. R. Lee, "Electron backscatter diffraction investigation of length-fast chalcedony in agate: implications for agate genesis and growth mechanisms," *Geofluids*, vol. 13, no. 1, pp. 32–44, 2013.

[51] X. Y. Gao and T. P. Zhao, "Late Mesozoic magmatism and Tectonic evolution in the Southern margin of the North China Craton," *Science China Earth Sciences*, vol. 60, no. 11, pp. 1959–1975, 2017.

[52] D. L. Whitney and B. W. Evans, "Abbreviations for names of rock-forming minerals," *American Mineralogist*, vol. 95, no. 1, pp. 185–187, 2010.

[53] M. M. Raith, R. Hoffbauer, B. Spiering, M. Shinoto, and N. Nakamura, "Melting behaviour of feldspar clasts in high-fired sue ware," *European Journal of Mineralogy*, vol. 28, no. 2, pp. 385–407, 2016.

[54] M. D. Foster, "Interpretation of the composition of Trioctahedral Micas," *Geological Survey Professional Paper*, vols. 354-B, pp. 11–49, 1960.

[55] Z. X. Zhou, "Chemical characteristics of Mafic mica in intrusive rocks and its geological meaning," *Acta Petrologica Sinica*, vol. 4, no. 3, pp. 63–73, 1988.